Article

Garnet-Based All-Ceramic Lithium Battery Enabled by $Li_{2.985}B_{0.005}OCl$ Solder

Hot-pressing — All Ceramic Lithium Battery

400 °C

Au interlayer
Li Anode

$Li_{2.985}B_{0.005}OCl$ $Li_{6.75}La_3Zr_{1.75}Ta_{0.25}O_{12}$ $LiCoO_2$

All Ceramic Lithium Battery Li/Ceramic Electrolyte/$LiCoO_2$

Capacity (mAh/g) vs Cycle number

Wuliang Feng,
Zhengzhe Lai,
Xiaoli Dong,
Panlong Li,
Yonggang Wang,
Yongyao Xia

yyxia@fudan.edu.cn

HIGHLIGHTS
Hot-press sintering is developed in densifying the all-ceramic lithium battery

$Li_{2.985}B_{0.005}OCl$ displays a high ionic conductivity and a low melting point

$Li_{2.985}B_{0.005}OCl$ layer is *in situ* coated on both garnet and $LiCoO_2$ uniformly

The strain/stress effects of the $LiCoO_2$ is released during charge/discharge

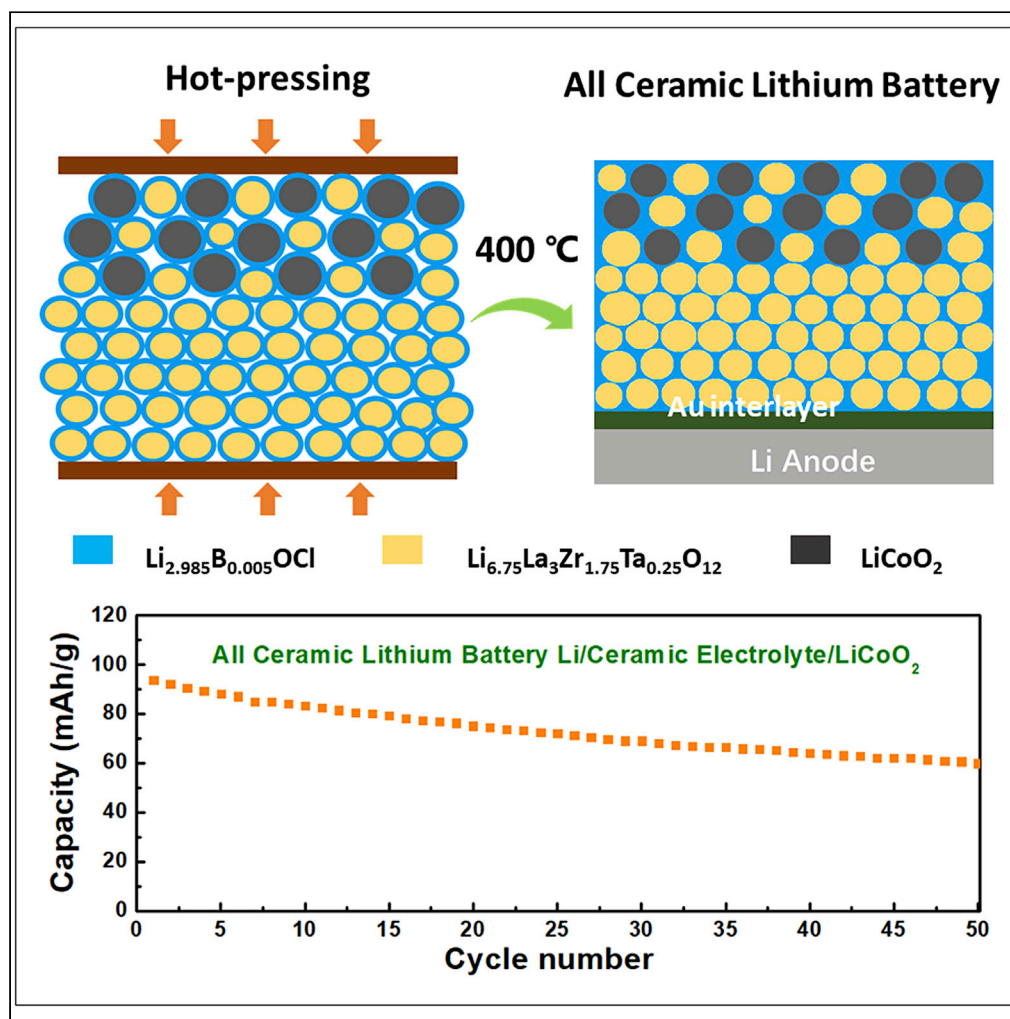## Article

Garnet-Based All-Ceramic Lithium Battery Enabled by Li$_{2.985}$B$_{0.005}$OCl Solder

Wuliang Feng,[1] Zhengzhe Lai,[1] Xiaoli Dong,[1] Panlong Li,[1] Yonggang Wang,[1] and Yongyao Xia[1,2,*]

SUMMARY

Garnet-based bulk-type all-ceramic lithium battery (ACLB) is considered to be highly safe, but its electrochemical performance is severely hindered by the huge cathode/electrolyte interfacial resistance. Here, we demonstrate an *in situ* coated Li$_{2.985}$B$_{0.005}$OCl as sintering solder, which is uniformly coated on both LiCoO$_2$ and Li$_7$La$_3$Zr$_2$O$_{12}$. With the low melting point (267°C) and high ionic conductivity (6.8 × 10^{-5} S cm^{-1}), the Li$_{2.985}$B$_{0.005}$OCl solder not only restricts La/Co interdiffusion, but also provides fast Li$^+$ transportation in the cathode. A low cathode/electrolyte interfacial resistance (386 Ω cm^2) is realized owing to the densification of the ACLB by hot-press sintering. The strain/stress of the LiCoO$_2$ is also released by the small elasticity modulus of Li$_{2.985}$B$_{0.005}$OCl, leading to a superior cycling stability. The study sheds light on the design of advanced garnet-based bulk-type ACLB by exploring proper solders with higher ionic conductivity, lower melting point, and smaller elasticity modulus.

INTRODUCTION

The all-ceramic lithium battery (ACLB) is regarded as the ultimate goal to exclude the safety concerns for Li-ion battery (Janek and Zeier, 2016; Zhang et al., 2018a, 2018b). To successfully achieve an ACLB with satisfied electrochemical performance, electrolyte/electrode interfacial problem is the most changing part rather than the ionic conductivity of the solid-state electrolytes (SSEs) (Jena, et al., 2018). Sulfide-based SSEs are soft enough to reduce the interfacial resistance just by high-pressure treatment. However, there remains a poor electrochemical stability against electrodes and a risk of toxic H$_2$S release (Han et al., 2016; Wenzel et al., 2016; Matthew et al., 2019; Wu et al., 2018). Very recently, halide-based SSEs Li$_3$MCl$_6$ (M = In, Y, Er) with ionic conductivity over 1 mS cm^{-1} have been developed, and the Young's modulus is also low enough to enable its bulk ACLB assembly without any heat treatment (Li et al., 2019a, 2019b; Schlem et al., 2019). Unfortunately, the halide SSEs are hygroscopic and also unstable with metal Li (Asano et al., 2018). Among all of the SSEs, garnet-type SSEs Li$_7$La$_3$Zr$_2$O$_{12}$ (LLZO) exhibit the widest electrochemical window against Li and a variety of cathodes, making it an attractive candidate for bulk-type ACLB (Zhao et al., 2019; Liu et al., 2018a, 2018b; Li et al., 2017).

Regardless of the lithiophobic layers on the surface, which lead to large Li/LLZO interfacial resistance, the issue has already been effectively solved by surface polishing (Sharafi et al., 2017; Wu et al., 2019) and interlayers (Han et al., 2017; Alexander et al., 2018; Feng et al., 2019; Huo et al., 2019; Fu et al., 2019) or composite anodes integrating (Lu et al., 2018; Wang et al., 2018). The area-specific resistance (ASR) has been reduced by three orders of magnitude, and Li dendrite can also be suppressed owing to the moderated Li stripping and plating environment (Li et al., 2018).

By contrast, there are few studies available in garnet-based bulk-type ACLB since the cathode/LLZO interface is the main obstacle (Park et al., 2016). The circumstance of cathode/LLZO interface is more complex than that of Li/LLZO, which includes (1) huge interfacial resistance due to the lack of contact between active materials and LLZO (Liu et al., 2017), (2) the formation of highly ionic resistive phase during sintering (Kim et al., 2011; Zhang et al., 2018a, 2018b), (3) and the cracks at the interface due to the volume change of the active materials (Okumura et al., 2016). Explorations have been done on enlarging the contact area of LLZO with active materials by building a 3D LLZO surface (Broek et al., 2016; Hänsel et al., 2016; Shoji et al., 2016), whereas the discharge capacities are still far from satisfied. Owing to the rigid character of the

[1]Department of Chemistry and Shanghai Key Laboratory of Molecular Catalysis and Innovative Materials, Institute of New Energy, Fudan University, Shanghai 200433, China

[2]Lead Contact

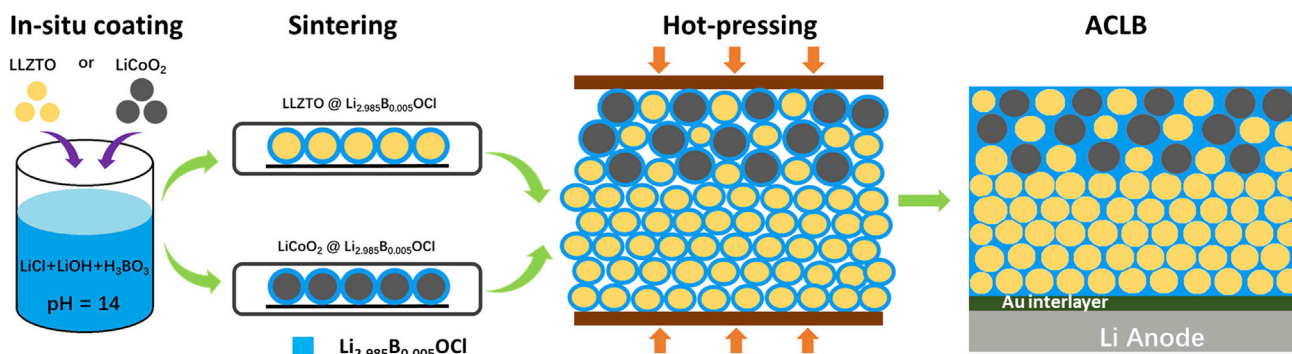*Correspondence: yyxia@fudan.edu.cn

https://doi.org/10.1016/j.isci.2020.101071

Figure 1. Schematic Diagram of Surface Coating of $Li_{2.985}B_{0.005}OCl$ and Assembling of ACLB

ceramic-to-ceramic interface, high-temperature sintering is an indispensable step to improve the contact of the active materials with LLZO. However, there remains a risk of forming Li^+-resistive interdiffusion phase of $LaXO_3$ (X = Ni, Co, Mn) even at the temperature as low as 500°C (Vardar et al., 2018). To simultaneously improve the contact of the active materials with LLZO and suppress the interdiffusion phase, solders such as Li_3BO_3, $Li_{2.3}C_{0.7}B_{0.3}O_3$, and $Li_{2.2}C_{0.8}B_{0.2}O_3$ have been applied to the ACLBs (Park et al., 2016; Ohta et al., 2013, 2014; Han et al., 2018; Okumura et al., 2016). In addition, $0.44LiBO_2.0.56LiF$ and $Li_3BO_3.ITO$ have also been introduced to synthesize the all-ceramic cathodes (Chen et al., 2014; Liu et al., 2018a, 2018b). However, the ionic conductivities of the solders are in the 10^{-6} S cm^{-1} scale or even lower, which can be a constraint factor for Li^+ transport. Moreover, the melting point of the solder is much higher than 500°C, which leads to even higher sintering temperature. Thus, the cathode still suffers from forming interdiffusion phase once there remains a direct contact of the active materials with LLZO.

In the present work, we proposed a trivalent element doped $Li_{2.985}B_{0.005}OCl$ anti-perovskite as an effective solder for the ACLB, which demonstrated not only an ionic conductivity more than one order of magnitude higher than the present candidates (6.8×10^{-5} S cm^{-1}), but also a melting point as low as 267°C. A novel alkaline aqueous solution-based *in situ* coating of $Li_{2.985}B_{0.005}OCl$ on both $Li_{6.75}La_3Zr_{1.75}Ta_{0.25}O_{12}$ (LLZTO) and $LiCoO_2$ (LCO) was introduced, in which a $Li_{2.985}B_{0.005}OCl$ layer was uniformly coated on the particle surface. Both Li^+/H^+ exchange suppression in LLZTO and LCO/LLZTO thorough segregation were realized. The critical current density (CCD) of the $LLZTO@Li_{2.985}B_{0.005}OCl$ composited electrolyte (CE) was improved from 0.6 to 0.8 mA/cm^2 owing to the reduced electronic conductivity at the grain boundary. The ACLB was assembled in a simple way by co-hot-press sintering of the CE and the cathode at 400°C, which displayed a smaller impedance than the traditional cold-press sintered counterpart. Attributing the lower elasticity modulus, $Li_{2.985}B_{0.005}OCl$ is soft enough to release more strain/stress effects of the LCO during charge/discharge, and the $Li_{2.985}B_{0.005}OCl$ soldered ACLB demonstrated higher capacity and cycling stability than the Li_3BO_3 and LiF soldered counterparts.

RESULTS AND DISCUSSION

$Li_{2.985}B_{0.005}OCl$ *In Situ* Coating and the ACLB Assembling

As illustrated in Figure 1, $Li_{2.985}B_{0.005}OCl$ was *in situ* coated on LCO and LLZTO in alkaline aqueous solution. Li^+/H^+ exchange reaction in LLZTO can be avoided by increasing the pH value to 14 by adjusting the stoichiometric amounts of the starting materials (LiCl, LiOH, and H_3BO_3), and the concentration of the LiOH should be over 1 M to ensure the required pH value. The reaction equation based on the starting material is $Li + 1.985 LiOH + 0.005 H_3BO_3 \rightarrow Li_{2.985}B_{0.005}OCl + H_2O$. The coated LLZTO is in cubic phase and no $La_2Zr_2O_7$ lithium-devoid phases can be indexed, indicating the successfully suppressed Li^+/H^+ exchange (Figure S1A). To acquire the $Li_{2.985}B_{0.005}OCl$ anti-perovskite on the surface, the coated LCO and LLZTO were sintered at 350°C under vacuum. As the X-ray photoelectron spectra shown in Figure S2, Cl-O bonding can be found in both Cl 2p and O 1s core levels, indicating the formation of the $Li_{2.985}B_{0.005}OCl$ anti-perovskite. In regard to the ACLB assembly, considering that the conventional synthesized LLZTO pellet (sintered over 1,000°C) is fragile and unable to sustain any high pressure, the CE was co-hot-pressed together with the cathode at 400°C, to simultaneously melt the $Li_{2.985}B_{0.005}OCl$ solder in cathode and the CE. Finally, Au thin film was deposited on one side of the CE to improve the wettability of molten Li and reduce the interfacial resistance.
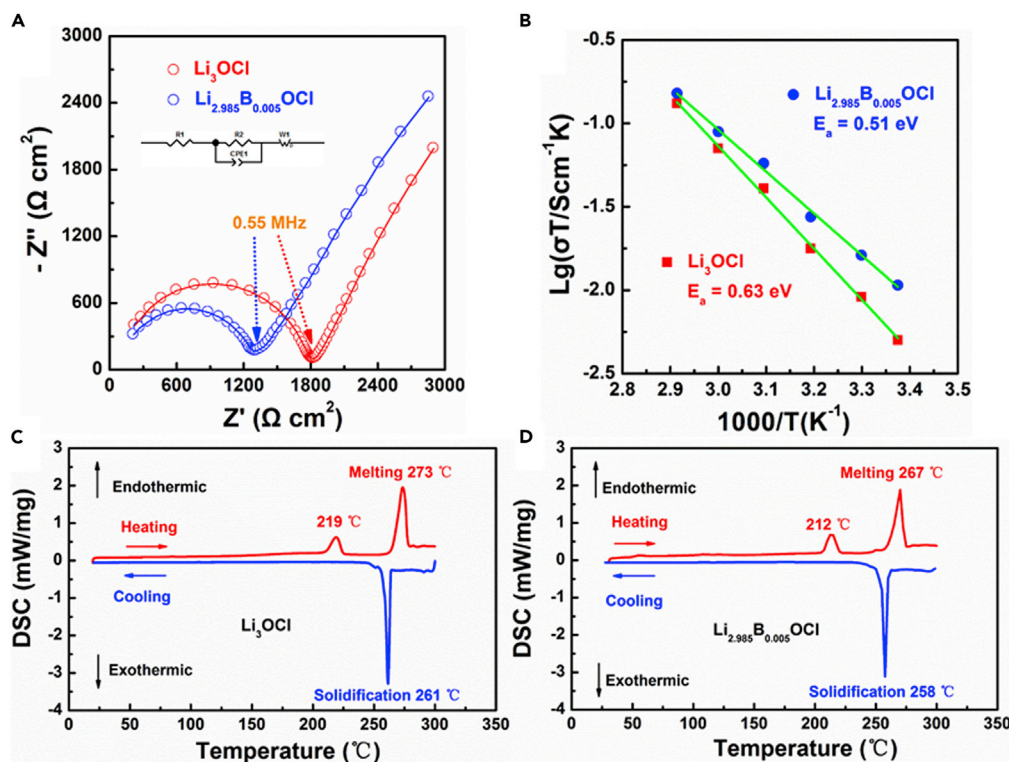
Figure 2. Characterization of the Anti-Perovskites

(A) Nyquist plot of the anti-perovskites without and with B^{3+} doping.

(B) Arrhenius plot of the anti-perovskites without and with B^{3+} doping.

(C and D) DSC data of the (C) Li_3OCl and (D) $Li_{2.985}B_{0.005}OCl$ electrolytes.

Characterization of the Anti-perovskite Electrolytes

Based on the conventional Li_3OCl anti-perovskite electrolyte, trivalent element B^{3+} was introduced to further increase the ionic conductivity of the solder. According to the EIS profiles in Figure 2A, the ionic conductivity of Li_3OCl and $Li_{2.985}B_{0.005}OCl$ are 4.9×10^{-5} and 6.8×10^{-5} S cm^{-1} respectively. As shown in the Arrhenius plot (Figure 2B), the activation energy for Li$^+$ diffusion was decreased from 0.63 to 0.51 eV by the vacancy creation, which led to the faster ionic transportation. Herein the molecular formula (i.e., $Li_{2.985}B_{0.005}OCl$) is only used to briefly describe the material composition. As the prepared material shows the amorphous characteristics with a low diffraction peak density in XRD pattern (Figure S1B), at the current stage, it is very hard to confirm the crystalline framework of the B-modified Li_3ClO. However, it should be noted that B-doping is not the key point of the present work, and thus we do not give further discussion on this point. Different kinds of alkali metal cations have been doped to improve the ionic conductivity of the anti-perovskite by creating more vacancies in the cation sublattice (Braga et al., 2014). With the doping of a higher-valent cation B^{3+}, more vacancies and Li$^+$ transport paths can be potentially created by coordinating the charge balance. The structural changes and melting and solidification points are characterized by differential scanning calorimetry (DSC). The anti-perovskite without dopant shows a phase transition peak at 219°C, a melting peak at 273°C, and a solidification peak at 261°C (Figure 2C). With B^{3+} doping, the phase transition, melting, and solidification points are 7°C, 6°C, and 3°C lower than that of Li_3OCl (Figure 2D). The melting and solidification points are presently the lowest among all of the solder for garnet-based ACLB and are essential to reduce the heat treatment from conventional 700°C to only 400°C.

Characterization of the *In Situ* Coating of $Li_{2.985}B_{0.005}OCl$

As the transmission electron microscopy (TEM) image illustrated in Figures 3A and 3B, the *in situ* coated $Li_{2.985}B_{0.005}OCl$ has covered all of the surface and every corner of LLZTO and LCO particles, which is vital to realize the thoroughly separated LLZTO and LCO. The mapping of Cl and Zr in Figures S3A–S3C demonstrated that the $Li_{2.985}B_{0.005}OCl$ is evenly coated. Comparing with Figures 3A and 3B, TEM of the pristine LLZTO (Figure S3D) and LCO (Figure S3F) shows that the particles are exposed without the coating layer. The cross-sectional scanning electron microscopy (SEM) images in Figures 3C and 3D compare the porosity
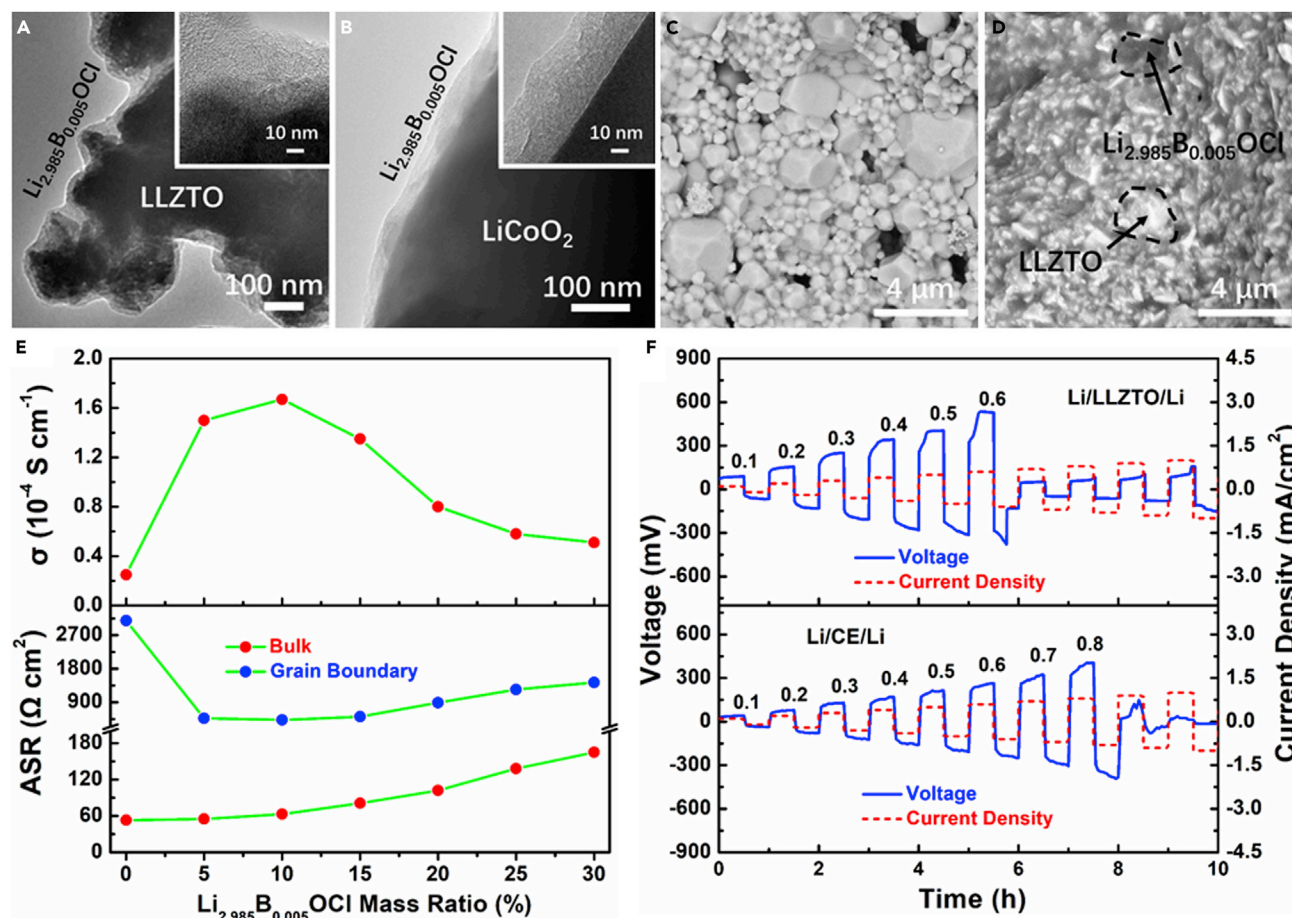
Figure 3. Characterization of the Composited Electrolyte
(A and B) TEM images of the coated (A) LLZTO and (B) LCO particles.
(C and D) Cross-sectional SEM images of the (C) LLZTO and (D) LLZTO@$Li_{2.985}B_{0.005}$OCl electrolytes being hot pressed at 400°C.
(E) Li$^+$ conductivity, ASR of the bulk and grain boundary as a function of $Li_{2.985}B_{0.005}$OCl mass ratio.
(F) CCD testing of the Li/LLZTO/Li and Li/CE/Li symmetric cells.

of the pristine LLZTO and the CE that were treated at 400°C. Evident holes can be found in the pristine LLZTO, whereas the $Li_{2.985}B_{0.005}$OCl soldered LLZTO is much denser and no holes can be found. To study the influence of the $Li_{2.985}B_{0.005}$OCl mass ratio on the electrochemical performance of the CE, the staring materials of LiCl, LiOH, and H_3BO_3 were adjusted to different concentrations to get the CE with $Li_{2.985}B_{0.005}$ClO mass ratio from 5% to 30%. The EIS profiles of the CE with different $Li_{2.985}B_{0.005}$OCl mass ratio are demonstrated in Figure S4 and the fitted results are displayed in Table S1. Owing to the large amounts of voids, the pristine LLZTO shows the least ionic conductivity. With the soldering of $Li_{2.985}B_{0.005}$OCl, the ionic conductivity increased to the maximum when the mass ratio was 10% (2.09×10^{-4} S cm^{-1}). However, the ionic conductivity decreased slowly with the further increasing of the mass ratio. Figure 3E gives more visualized relationship of the ionic conductivity and the ASR as a function of $Li_{2.985}B_{0.005}$OCl mass ratio. The remarkable increased ionic conductivity from 0% to 10% mass ratio corresponds to the evidently reduced grain boundary resistance, which is due to the compactly soldered LLZTO particles. The subsequently reduced ionic conductivity of CE is probably due to the relatively lower ionic conductivity of $Li_{2.985}B_{0.005}$OCl than that of LLZTO, which increased the grain boundary resistance of CE. It is also worth noticing that the bulk resistance of the CE kept increasing constantly, which is also due to the relatively lower ionic conductivity of $Li_{2.985}B_{0.005}$OCl.

It has been well known that the high electronic conductivity at the grain boundary of SSE is crucial for Li dendrite growth according to Wang's demonstration (Han et al., 2019). Consequently, reducing the electronic conductivity at the grain boundary will play an important role in Li dendrite suppression. Direct

current polarization at different voltages from 0.4 to 0.8 V was tested to study the electronic conductivity of $Li_{2.985}B_{0.005}ClO$ (Figure S6A) and LLZTO (Figure S6B), and the equilibrium current response in Figures S5A and S5B illustrated the smaller electronic conductivity of $Li_{2.985}B_{0.005}ClO$ (5.2×10^{-9} S cm^{-1}) than that of LLZTO (9.6×10^{-8} S cm^{-1}). To evaluate the ability of Li dendrite suppression by reducing the electronic conductivity at the grain boundary, Li/LLZTO/Li and Li/CE/Li symmetric cells were tested under the direct current density stepping from 0.1 to 1.0 mA/cm^2. Apart from the high electronic conductivity in the grain boundary, the interfacial resistance of the Li/electrolyte interface also plays an important role in Li dendrite growth. It is known that the Li/antiperovskite interfacial resistance is smaller than that of Li/garnet (Tian et al., 2018). Au modification layer was deposited to eliminate the difference on the Li/electrolyte interfacial resistance. Moreover, both Li/CE and Li/garnet interfaces could be further modified to promote the Li wettability by this Au modification layer. With the modification of Au interlayer, intimate contact of Li/LLZTO and Li/CE was obtained (Figures S7A and S7B). The two interfacial resistances were in the same level, which can be seen from the second arc in the EIS profile, and calculated to be 226 Ω cm^2 for Li/LLZTO and 208 Ω cm^2 for Li/CE (Figure S7C). The pristine LLZTO was sintered at 1,100°C to reduce the ionic transport resistance at the grain boundary, and a similar overall ionic conductivity was also obtained according to the first arc in the EIS profile. As is displayed in Figure 3F, the Li/LLZTO/Li symmetric cell displays a CCD of 0.6 mA/cm^2, whereas the CCD of Li/CE/Li symmetric cell increased to 0.8 mA/cm^2, indicating that the low electronic conductivity of $Li_{2.985}B_{0.005}OCl$ at the grain boundary of LLZTO played an important role in Li dendrite suppression. After CCD test, the symmetric cells were dissected and Li dendrites can be found in the grain boundary in both LLZTO and CE (Figures S7D and S7E).

Characterization of the Cathode/Electrolyte Interfaces

The $LCO@Li_{2.985}B_{0.005}OCl$ and CE were made into slurry and spin-coated on the pre-cold pressed CE pellet. As the cross-sectional SEM image demonstrated in Figure 4A, the as-coated cathode is porous. After being hot-pressed at 400°C, the cathode was soldered compactly and no voids can be found (Figure 4B). By contrast, the conventional cold-press sintered ACLB leaves a large sum of voids not only at the interface, but also inside the cathode (Figure 4C), which could lead to a larger impedance. To make a closer comparison of the hot-press sintered cathode/CE interface and the conventional cold-press sintered cathode/LLZTO interface, cathode/electrolyte/cathode symmetric cells were assembled and tested at 90°C. According to the second arcs in Figure 4D, the ASR of the cathode/LLZTO and the cathode/CE interfacial resistances are calculated to be 769 and 386 Ω cm^2, indicating the superiority of the hot-pressing treatment by densifying the cathode and reducing the voids at the interface. Figure 4E displays the impedance of the LCO/electrolyte/Li full cells without and with hot pressing at 90°C. It is obvious that the conventional cold-press sintered ACLB possesses much huger impedance than the hot-pressed one, which is mainly due to the larger cathode/LLZTO interfacial resistance. Figure 4F illustrates the elemental line scanning of the cathode/CE interfaces. No mutual diffusion of Co and La at the interface can be indexed, indicating the successfully suppressed La_2CoO_4 phase through $Li_{2.985}B_{0.005}OCl$ *in situ* coating and the low sintering temperature.

Electrochemical Performance of the ACLBs with Different Solders

Three different kinds of ACLBs were assembled by hot pressing to evaluate the effects of the different solders on each ACLB. The sintering temperatures of Li_3BO_3 and LiF soldered ACLBs were adjusted to 700°C and 900°C, which were higher than each melting point. According to Ohsuku's research, there is a phase transition from rhombohedral to monoclinic in LCO at the open-circuit voltage of 4.12 V (Ohzuku and Ueda, 1994). Consequently, the charging cutoff potential was set to be 4.1 V (versus Li/Li$^+$) to avoid the unwanted phase transition. Figures 5A–5C shows the initial charge/discharge curves of the ACLBs at 90°C with $Li_{2.985}B_{0.005}OCl$, Li_3BO_3, and LiF solders. $Li_{2.985}B_{0.005}OCl$ soldered ACLB delivered the highest initial discharge capacity of 93.8 mAh/g and a coulombic efficiency of 88.6% (Figure 5A), whereas the Li_3BO_3 soldered counterpart displays a much smaller initial discharge capacity of 79.3 mAh/g and a coulombic efficiency of 81.7% (Figure 5B). In comparison, LiF soldered ACLB displays the lowest initial discharge capacity of 76.4 mAh/g, and the coulombic efficiency is also as low as 80.2% (Figure 5C). There are two main reasons that probably lead to the inferior electrochemical performance of the ACLB with Li_3BO_3 and LiF solders. First, as the EIS profiles shown in Figure S8, the ionic conductivities of two solders are too low to provide a satisfactory Li$^+$ transportation environment, which are only 2.3×10^{-6} (Li_3BO_3) and 6.7×10^{-7} S cm^{-1} (LiF). Second, owing to their insolubility, Li_3BO_3 and LiF were coated on LCO and LLZTO by mechanical ball milling, which probably leads to an unthoroughly segregated LCO and LLZTO. The soldering temperature for the two ACLBs are high enough to form the highly ionic resistive La_2CoO_4 phase once there remains a direct contact between LCO and LLZTO, and then leads to the degradation of the LCO/LLZTO interfaces. As the cycling of the three ACLBs shown in Figure 5D, $Li_{2.985}B_{0.005}OCl$ soldered ACLB displays
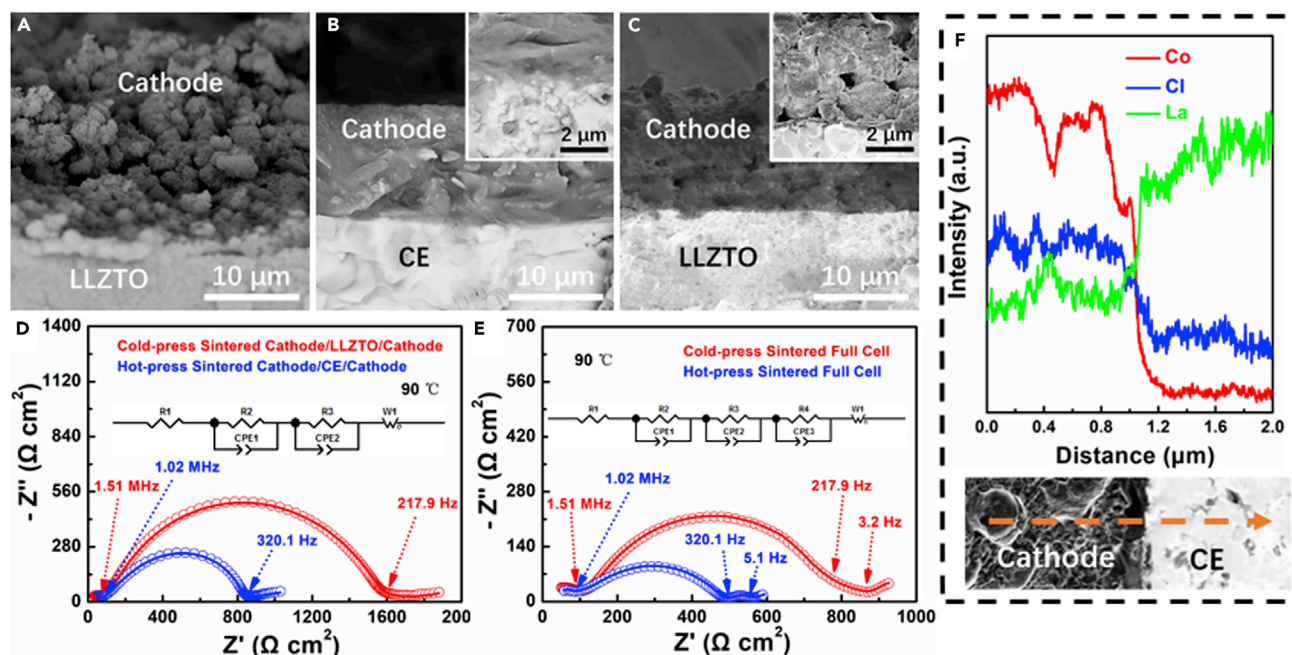
Figure 4. The Cathode/Electrolyte Interfaces Characterization
(A–C) Cross-sectional SEM image of cathode/electrolyte interface (A) before and (B) after hot press and (C) after conventional cold-pressed sintering.
(D) EIS profiles of the cold-press sintered and hot-press sintered cathode/electrolyte/cathode symmetric cells at 90°C.
(E) EIS profiles of the cold-press sintered and hot-press sintered LCO/electrolyte/Li full cells at 90°C.
(F) Elemental line scanning of the cathode/CE interfaces after hot pressing. The imaginary line corresponds to the scanning region.

the most stable performance of 50 cycles, whereas the Li_3BO_3 and LiF show not only lower discharge capacities but also faster degradation.

Assembly information and electrochemical performances of the garnet-based ACLBs with different solders are summarized in Table S2. It is obvious that $Li_{2.985}B_{0.005}OCl$ displays the highest ionic conductivity. Moreover, the $Li_{2.985}B_{0.005}OCl$ soldered ACLB demonstrates the lowest sintering temperature, the highest initial coulombic efficiency, and the longest cycle life. The improved coulombic efficiency is probably because there contains no organic binder like ethyl cellulose, as the decomposition of organolithium compounds that were produced during the sintering is responsible for the low initial coulombic efficiency in the conventional garnet-based ACLBs Ohta et al., 2014. The $Li_{2.985}B_{0.005}OCl$ soldered ACLB was also cycled in 25°C to evaluate its room temperature performance. But according to the initial charge/discharge curves and the cycling performance in Figures 5E and 5F, the ACLB demonstrates a smaller initial discharge capacity (71.3 mAh/g) and a faster degradation than that was cycled at 90°C. The phenomenon is mainly due to the larger room temperature impedance, which is about 5-fold increased than that at 90°C (Figure S9).

***In Situ* EIS Profiles of the ACLBs at 90°C**

For a more detailed investigation on the cycling stabilities, *in situ* impedances of the three kinds of ACLBs during the initial cycles have been tested and analyzed. As illustrated in Figures 6A–6C, the bulk and grain boundary resistances of each electrolyte show negligible changes, indicating that the solders are highly stable during the galvanostatic charge and discharge. With the decreasing of the ionic conductivity of the solders, the ASR of the grain boundary increased slightly, which are about 98 Ω cm^2 for $Li_{2.985}B_{0.005}OCl$, 116 Ω cm^2 for Li_3BO_3, and 143 Ω cm^2 for LiF. It is interesting to find that all of the anode/electrolyte interfacial resistances display an evident decrease during charge and increase during discharge. The initial decreasing can be explained as the vanished interfacial holes or voids that were filled by the platted Li, which provided more intimate contact between Li and the electrolytes. The subsequent impedance augment can be comprehended as the interfacial gaps that were created by the stripped Li (Yang et al., 2018).
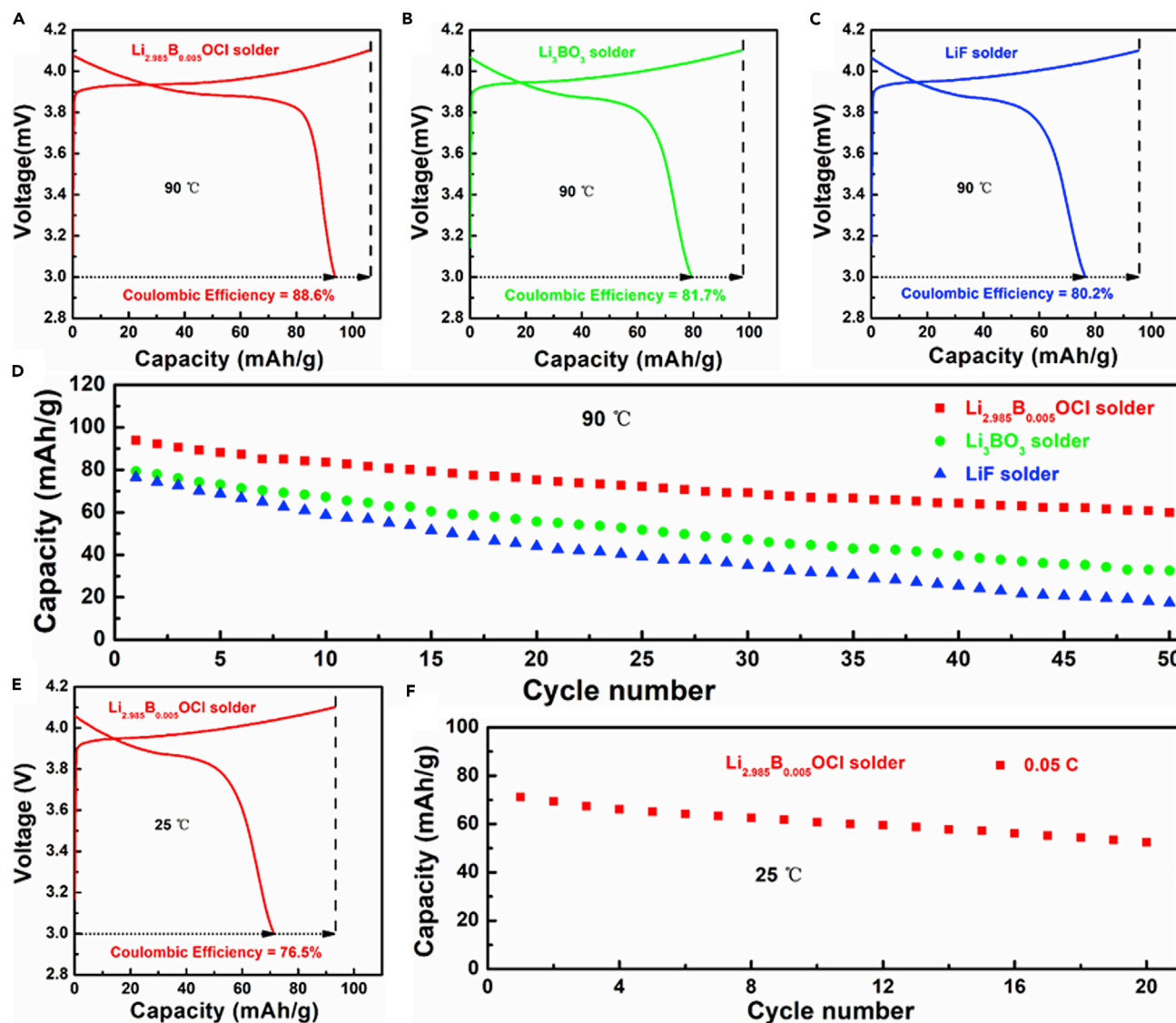
Figure 5. Electrochemical Performance of the Full Cells

(A–C) Initial charge/discharge curves of the ACLBs at 90°C with (A) $Li_{2.985}B_{0.005}OCl$, (B) Li_3BO_3, and (C) LiF solders.

(D) Cycling of the ACLBs.

(E and F) (E) Initial charge/discharge curves, and (F) cycling of the $Li_{2.985}B_{0.005}OCl$ soldered ACLBs at 25°C.

Moreover, The ASR of the cathode/electrolyte interface increased with the decreasing of the ionic conductivity of the solders, which are about 386 Ω cm^2 for $Li_{2.985}B_{0.005}OCl$, 595 Ω cm^2 for Li_3BO_3, and 912 Ω cm^2 for LiF before cycling. It is also worth noticing that all of the cathode/electrolyte interfacial resistances increased to some extent after the initial cycle, which are 4.6%, 11.3%, and 7.9% for $Li_{2.985}B_{0.005}OCl$, Li_3BO_3, and LiF, respectively. Since it is known that the length of the c-axis and the a-axis in LCO changes conversely during charge/discharge, Asano et al., 2018 due to the rigid solid to solid contacts between LCO and the solders, the ASR augments can be explained as the Griffith cracks that were generated by the strain/stress of the LCO during charge/discharge. But according to the elasticity modulus of the solders in Table S3, $Li_{2.985}B_{0.005}OCl$ displays the smallest elasticity modulus (7.8 GPa). In other words, $Li_{2.985}B_{0.005}OCl$ is soft enough to release more strain/stress effects of the LCO than that of Li_3BO_3 and LiF, which resulted in the smaller ASR augment, higher initial coulombic efficiency, and more stable cycling. Comparatively, Li_3BO_3 and LiF show higher elasticity modulus of 20.5 and 11.9 GPa, which correspond with each ASR augment. The stiffer nature of the solders will lead to more cracks at the interfaces and deteriorate the cycling stabilities.
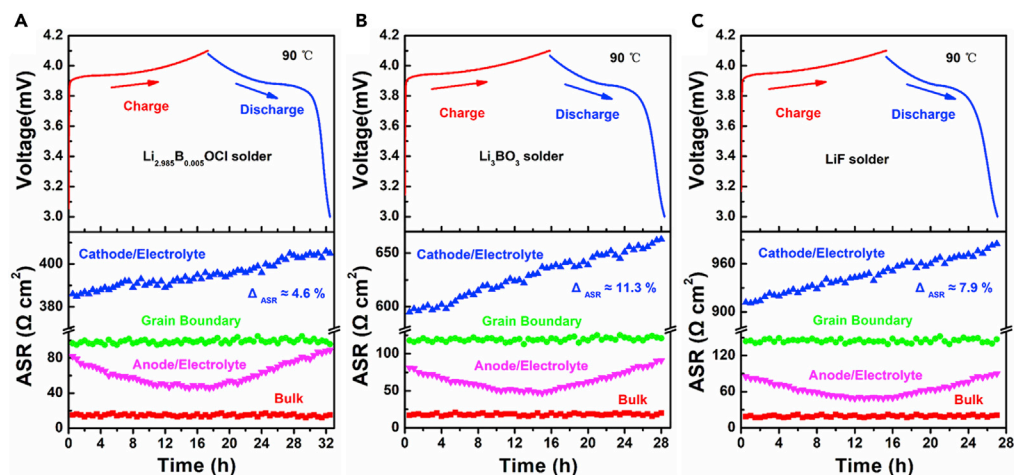
Figure 6. *In Situ* EIS Profiles of the ACLBs at 90°C with Different Solders during the Initial Cycle
(A) $Li_{2.985}B_{0.005}OCl$, (B) Li_3BO_3, and (C) LiF.

Conclusion

$Li_{2.985}B_{0.005}OCl$ anti-perovskite electrolyte was applied as sintering solder for garnet-based bulk-type ACLB, whose conductivity is as high as 6.8×10^{-5} S cm^{-1} and melting point is as low as 267°C. A novel alkaline aqueous solution-based *in situ* coating process was introduced to thoroughly segregate the LLZTO and LCO. Hot-press sintering was introduced to densify both CE and the cathode, and a low cathode/electrolyte ASR of 386 Ω cm^2 was realized. Attributing to the smaller elasticity modulus, $Li_{2.985}B_{0.005}OCl$ is also soft enough to release more strain/stress effects than the Li_3BO_3 and LiF counterparts, leading to a higher initial coulombic efficiency and more stable cycling. In addition, Li dendrite can be suppressed by the reduced electronic conductivity at the grain boundary. With the approaches that turned out to be effective, we believe that the improvements of the garnet-based bulk-type ACLB can be realized by integrating a solder with higher ionic conductivity, lower melting point, and smaller elasticity modulus.

Limitations of the Study

The garnet-based all-ceramic lithium battery is very fragile after hot pressing, which needs to be very carefully held during the electrochemical characterization. Moreover, the active material loading is still very low. Enhancing the loading of the composited cathode will lead to higher interfacial resistance and deteriorates the cycling stability. Electronic conductors such as carbon nano tubes (CNTs) or Super-P need to be added once the cathode loading is increased.

METHODS

All methods can be found in the accompanying Transparent Methods supplemental file.

DATA AND CODE AVAILABILITY

All data, models, and code generated or used during the study appear in the submitted article.

SUPPLEMENTAL INFORMATION

Supplemental Information can be found online at https://doi.org/10.1016/j.isci.2020.101071.

ACKNOWLEDGMENTS

AUTHOR CONTRIBUTIONS

Y.X. and W.F. conceived idea and designed the experiments. Y.X. and Y.W. directed the project. W.F. and Z.L. carried out the experiments. W.F. wrote the paper. X.D. and P.L. carried out the data analysis. Y.X. is the corresponding author. All authors discussed the results and commented on the manuscript.

DECLARATION OF INTERESTS

The authors declare no competing interests.

REFERENCES

Alexander, G., Patra, S., Raj, S., Sugumar, M., Din, M., and Murugan, R. (2018). Electrodes-electrolyte interfacial engineering for realizing room temperature lithium metal battery based on garnet structured solid fast Li^+ conductors. J. Power Sources 396, 764–773.

Asano, T., Sakai, A., Ouchi, S., Sakaida, M., Miyazaki, A., and Hasegawa, S. (2018). Solid halide electrolytes with high lithium-ion conductivity for application in 4 V class bulk-type all-solid-state batteries. Adv. Mater. 30, 1803075.

Braga, M., Ferreira, J., Stockhausen, V., Oliveira, J., and Azab, A. (2014). Novel Li_3ClO based glasses with superionic properties for lithium batteries. J. Mater. Chem. A 2, 5470–5480.

Broek, J., Afyon, S., and Rupp, J. (2016). Interface-engineered all-solid-state Li-ion batteries based on garnet-type fast Li^+ conductors. Adv. Energy Mater. 6, 1600736.

Chen, K., Shen, Y., Zhang, Y., Lin, Y., and Nan, C. (2014). High capacity and cyclic performance in a three-dimensional composite electrode filled with inorganic solid electrolyte. J. Power Sources 249, 306–310.

Feng, W.L., Dong, X.L., Lai, Z.Z., Zhang, X.Y., Wang, Y.G., Wang, C.X., Luo, J.Y., and Xia, Y.Y. (2019). Building an interfacial framework: Li/garnet interface stabilization through a Cu_6Sn_5 layer. ACS Energy Lett. 4, 1725–1731.

Fu, J., Yu, P.F., Zhang, N., Ren, G.X., Zheng, S., Huang, W.C., Long, X.H., Li, H., and Liu, X.S. (2019). In situ formation of a bifunctional interlayer enabled by a conversion reaction to initiatively prevent lithium dendrites in a garnet solid electrolyte. Energy Environ. Sci. 12, 1404–1412.

Han, F., Zhu, Y., He, X., Mo, Y., and Wang, C. (2016). Electrochemical stability of $Li_{10}GeP_2S_{12}$ and $Li_7La_3Zr_2O_{12}$ solid electrolytes. Adv. Energy Mater. 6, 1501590.

Han, X., Gong, Y., Fu, K., He, X.F., Hitz, G.T., Dai, J.Q., Pearse, A., Liu, B.Y., Wang, H., Rublo, G., et al. (2017). Negating interfacial impedance in garnet-based solid-state Li metal batteries. Nat. Mater. 16, 572–579.

Han, F., Yue, J., Chen, C., Zhao, N., Fan, X.L., Ma, Z.H., Gao, T., Wang, F., Guo, X.X., and Wang, C.S. (2018). Interphase engineering enabled all-ceramic lithium battery. Joule 2, 497–508.

Han, F., Westover, A.S., Yue, J., Fan, X.L., Wang, F., Chi, M.F., Leonard, D.N., Dudney, N.J., Wang, H., and Wang, C.S. (2019). High electronic conductivity as the origin of lithium dendrite formation within solid electrolytes. Nat. Energy 4, 187–196.

Hänsel, C., Afyon, S., and Rupp, J. (2016). Investigating the all-solid-state batteries based on lithium garnets and a high potential cathode - $LiMn_{1.5}Ni_{0.5}O_4$. Nanoscale 8, 18412–18420.

Huo, H., Chen, Y., Li, R.Y., Zhao, N., Luo, J., Silva, J., Mucke, R., Kaghazchi, P., Guo, X.X., and Sun, X.L. (2019). Design of a mixed conductive garnet/Li interface for dendrite-free solid lithium metal batteries. Energy Environ. Sci. 13, 127–134.

Janek, J., and Zeier, W.G. (2016). A solid future for battery development. Nat. Energy 1, 16141.

Jena, A., Meesala, Y., Hu, S., Chang, H., and Liu, R. (2018). Ameliorating interfacial ionic transportation in all-solid-state Li-ion batteries with interlayer modifications. ACS Energy Lett. 3, 2775–2795.

Kim, K., Iriyama, Y., Yamamoto, K., Kumazaki, S., Asaka, T., Tanabe, K., Fisher, C., Hirayama, T., Murugan, R., and Ogumi, Z. (2011). Characterization of the interface between $LiCoO_2$ and $Li_7La_3Zr_2O_{12}$ in an all-solid-state rechargeable lithium battery. J. Power Sources 196, 764–767.

Li, Y., Xu, B.Y., Xu, H.H., Duan, H.N., Lu, X.J., Xin, S., Zhou, W.D., Xue, L.G., Fu, G.T., Manthiram, A., et al. (2017). Hybrid polymer/garnet electrolyte with a small interfacial resistance for lithium-ion batteries. Angew. Chem. Int. Ed. 129, 771–774.

Li, Y., Chen, X., Dolocan, A., Cui, Z.M., Xin, S., Xue, L.G., Xu, H.H., Park, K., and Goodenough, J.B. (2018). Garnet electrolyte with an ultralow interfacial resistance for Li-metal batteries. J. Am. Chem. Soc. 140, 6448–6455.

Li, X., Liang, J.W., Chen, N., Luo, J., Adair, K.R., Wang, C.H., Banis, M.N., Sham, T.-K., Zhang, L., Zhao, S.Q., et al. (2019a). Water-mediated synthesis of a superionic halide solid electrolyte. Angew. Chem. Int. Ed. 58, 1–7.

Li, X., Liang, J.W., Luo, J., Banis, M.N., Wang, C.H., Li, W.H., Deng, S.X., Yu, C., Zhao, F.P., Hu, Y.F., et al. (2019b). Air-stable Li_3InCl_6 electrolyte with high voltage compatibility for all-solid-state batteries. Energy Environ. Sci. 12, 2665–2671.

Liu, B., Fu, K., Gong, Y.H., Yang, C.P., Yao, Y.G., Wang, Y.B., Wang, C.W., Kuang, Y.D., Pastel, G., and Xie, H. (2017). Rapid thermal annealing of cathode-garnet interface toward high temperature solid state batteries. Nano Lett. 17, 4917–4923.

Liu, Q., Geng, Z., Han, C.P., Fu, Y.Z., Li, S., He, Y.B., Kang, F.Y., and Li, B.H. (2018a). Challenges and perspectives of garnet solid electrolytes for all solid-state lithium batteries. J. Power Sources 398, 120–134.

Liu, T., Zhang, Y.B., Zhang, X., Wang, L., Zhao, S.X., Lin, Y.H., Shen, Y., Luo, J., Li, L.L., and Nan, C.W. (2018b). Enhanced electrochemical performance of bulk type oxide ceramic lithium batteries enabled by interface modification. J. Mater. Chem. A 6, 4649–4657.

Lu, Y., Huang, X., Ruan, Y.D., Wang, Q.S., Kun, R., Yang, J.H., and Wen, Z.Y. (2018). An in situ element permeation constructed high endurance Li–LLZO interface at high current densities. J. Mater. Chem. A 6, 18853–18858.

Matthew, L., Bai, Z.Y., Li, Y.J., Ma, L., Dai, A., Wang, X.F., Lin, D., Wu, T.P., Liu, P., Yang, L., et al. (2019). Electrochemically primed functional redox mediator generator from the decomposition of solid state electrolyte. Nat. Commun. 10, 1–9.

Ohta, S., Komagata, S., Seki, J., Saeki, T., Morishita, S., and Asaoka, T. (2013). All-solid-state lithium ion battery using garnet-type oxide and Li_3BO_3 solid electrolytes fabricated by screen-printing. J. Power Sources 238, 53–56.

Ohta, S., Seki, J., Yagi, Y., Kihira, Y., Tani, T., and Asaoka, T. (2014). Co-sinterable lithium garnet-type oxide electrolyte with cathode for all-solid-state lithium ion battery. J. Power Sources 265, 40–44.

Ohzuku, T., and Ueda, A. (1994). Solid-state redox reactions of $LiCoO_2$ (R3m) for 4 volt secondary lithium cells. J. Electrochem. Soc. 141, 2972–2976.

Okumura, T., Takeuchi, T., and Kobayashi, H. (2016). All-solid-state lithium-ion battery using $Li_{2.2}C_{0.8}B_{0.2}O_3$ electrolyte. Solid State Ionics 288, 248–252.

Park, K., Yu, B.C., Jung, J.W., Li, Y.T., Zhou, W.D., Gao, H.C., Son, S., and Goodenough, J.B. (2016). Electrochemical nature of the cathode interface for a solid-state lithium-ion battery: interface between $LiCoO_2$ and $Garnet Li_7La_3Zr_2O_{12}$. Chem. Mater. *28*, 8051–8059.

Schlem, R., Muy, S., Prinz, N., Banik, A., Yang, S.H., Zobel, M., and Zeier, W.G. (2019). Mechanochemical synthesis: a tool to tune cation site disorder and ionic transport properties of Li_3MCl_6 (M = Y, Er) superionic conductors. Adv. Energy Mater. *10*, 1903719.

Sharafi, A., Kazyak, E., Davis, A.L., Yu, S., Thompson, T., Siegel, D.J., Dasgupta, N.P., and Sakamoto, J. (2017). Surface chemistry mechanism of ultra-low interfacial resistance in the solid-state electrolyte $Li_7La_3Zr_2O_{12}$. Chem. Mater. *29*, 7961–7968.

Shoji, M., Munakata, H., and Kanamura, K. (2016). Fabrication of all-solid-state lithium-ion cells using three-dimensionally structured solid electrolyte $Li_7La_3Zr_2O_{12}$ pellets. Front. Energy Res. *4*, 1–7.

Tian, Y.J., Ding, F., Zhong, H., Liu, C., He, Y.B., Liu, J.Q., Liu, X.J., and Xu, Q. (2018).

$Li_{6.75}La_3Zr_{1.75}Ta_{0.25}O_{12}$@amorphous Li_3OCl composite electrolyte for solid state lithium-metal batteries. Energy Storage Mater. *14*, 49–57.

Vardar, G., Bowman, W.J., Lu, Q., Wang, J.Y., Chater, R.J., Aguadero, A., Seibert, R., Terry, J., Hunt, A., Waluyo, I., et al. (2018). Structure, chemistry, and charge transfer resistance of the interface between $Li_7La_3Zr_2O_{12}$ electrolyte and $LiCoO_2$ cathode. Chem. Mater. *30*, 6259–6276.

Wang, C.W., Xie, H., Zhang, L., Gong, Y.H., Pastel, G., Dai, J.Q., Liu, B.Y., Wachsman, E.D., and Hu, L.B. (2018). Universal soldering of lithium and sodium alloys on various substrates for batteries. Adv. Energy Mater. *8*, 1701963.

Wenzel, S., Randau, S., Leichtweiß, T., Weber, D.A., Sann, J., Zeier, W.G., and Janek, J. (2016). Direct observation of the interfacial instability of the fast ionic conductor $Li_{10}GeP_2S_{12}$ at the lithium metal anode. Chem. Mater. *28*, 2400–2407.

Wu, F., Fitzhugh, W., Ye, L., Ning, J., and Li, X. (2018). Advanced sulfide solid electrolyte by core-shell structural design. Nat. Commun. *9*, 1–11.

Wu, J., Pu, B.W., Wang, D., Shi, S.Q., Zhao, N., Guo, X.X., and Guo, X. (2019). In situ formed

shields enabling Li_2CO_3-free solid electrolytes: a new route to uncover the intrinsic lithiophilicity of garnet electrolytes for dendrite-free Li-metal batteries. ACS Appl. Mater. Interfaces *11*, 898–905.

Zhang, Z.Z., Shao, Y.J., Lotsch, B., Hu, Y.S., Li, H., Janek, J., Nazar, L.F., Nan, C.W., Maier, J., Armand, M., and Chen, L.Q. (2018a). New horizons for inorganic solid state ion conductors. Energy Environ. Sci. *11*, 1945–1976.

Yang, C., Xie, H., Ping, W.W., Fu, K., Liu, B.Y., Rao, J.C., Dai, J.Q., Wang, C.W., Pastel, G., and Hu, L.B. (2018). An electron/ion dual-conductive alloy framework for high rate and high-capacity solid-state lithium-metal batteries. Adv. Mater. *31*, 1804815.

Zhang, N., Long, X.H., Wang, Z., Yu, P.F., Han, F.D., Fu, J.M., Ren, G.X., Wu, Y.R., Zheng, S., Huang, W.C., et al. (2018b). Mechanism study on the interfacial stability of a lithium garnet type oxide electrolyte against cathode materials. ACS Appl. Energy Mater. *1*, 5968–5976.

Zhao, N., Khokhar, W., Bi, Z.J., Shi, C., Guo, X.X., Fan, L.Z., and Nan, C.W. (2019). Solid garnet batteries. Joule *3*, 1–10.

Supplemental Information

Garnet-Based All-Ceramic

Lithium Battery Enabled

by Li$_{2.985}$B$_{0.005}$OCl Solder

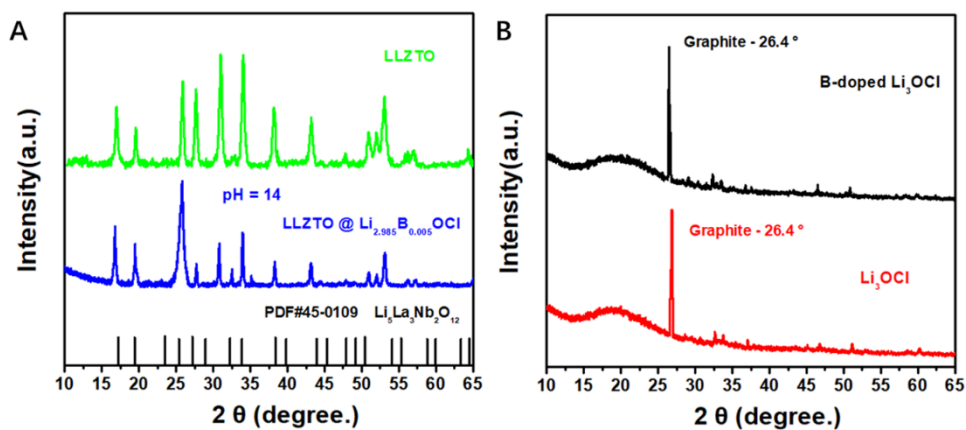Wuliang Feng, Zhengzhe Lai, Xiaoli Dong, Panlong Li, Yonggang Wang, and Yongyao Xia

Figure S1. XRD pattern of the doped and undoped anti-perovskites, pristine LLZTO and the coated LLZTO, related to Figure 1.

(A) The pristine LLZTO and the in-situ coated LLZTO.

(B) The doped and undoped Li_3OCl.

A tiny amount of graphite was mixed in the anti-perovskites to adjust the spectral shifts due to the test error between the doped and undoped Li_3ClO.
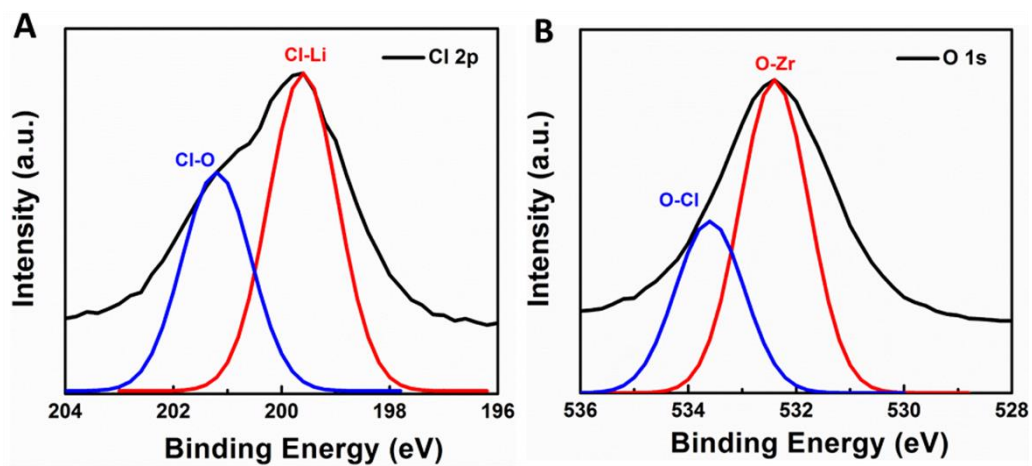
Figure S2. XPS spectra of $Li_{2.985}B_{0.005}OCl$ coated LLZTO, related to Figure 2.

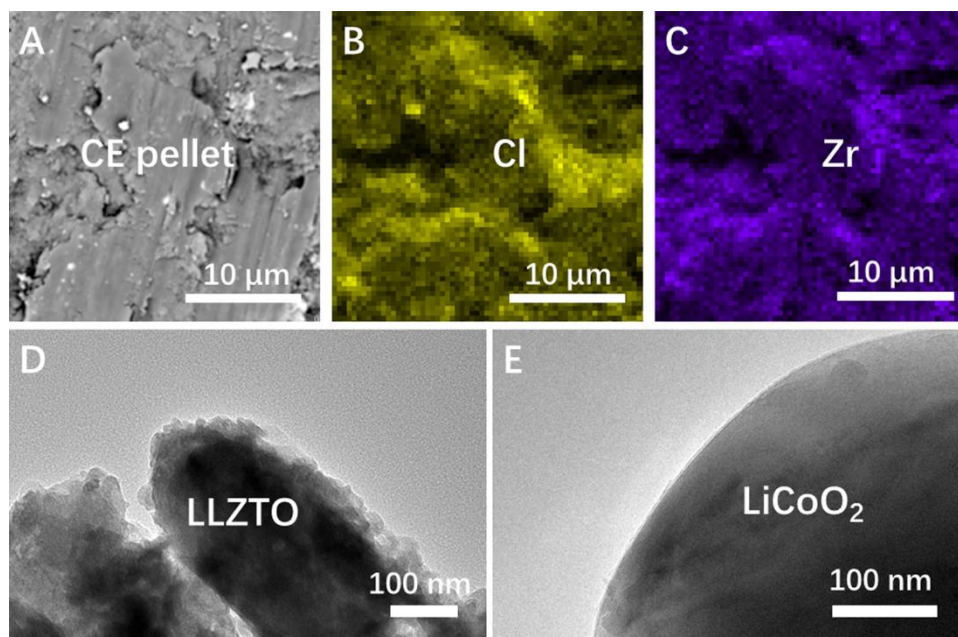(C) The core-level of Cl 2p.

(D) The core-level of O 1s.

Figure S3. Mapping of the composited electrolyte, TEM image of the pristine LLZTO and the LCO particles, related to Figure 3.

(A) SEM image of the surface of the CE pellet.

(B) Mapping of Cl.

(C) Mapping of Zr.

(D) TEM image of the pristine LLZTO.

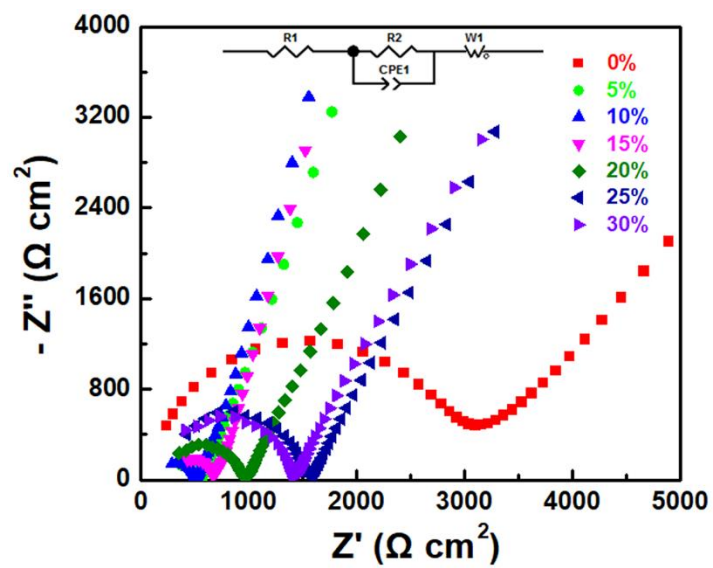(E) TEM image of the LCO particles.

Figure S4. EIS profiles of the CE with different Li$_{2.985}$B$_{0.005}$OCl mass ratios, related to Figure 3.

Table S1. Fitting results of the EIS profiles of the CE with different Li$_{2.985}$B$_{0.005}$OCl mass ratios, related to Figure 3.

Li$_{2.985}$B$_{0.005}$OCl Mass Ratio (%)	ASR$_{bulk}$ (Ω cm^2)	ASR$_{grain\ boundary}$ (Ω cm^2)	Ionic Conductivity (S cm^{-1})
0	53	3092	0.31 $\times$ 10^{-4}
5	55	471	1.89 $\times$ 10^{-4}
10	63	426	2.09 $\times$ 10^{-4}
15	81	511	1.69 $\times$ 10^{-4}
20	102	889	1.01 $\times$ 10^{-4}
25	138	1243	0.73 $\times$ 10^{-4}
30	165	1429	0.64 $\times$ 10^{-4}

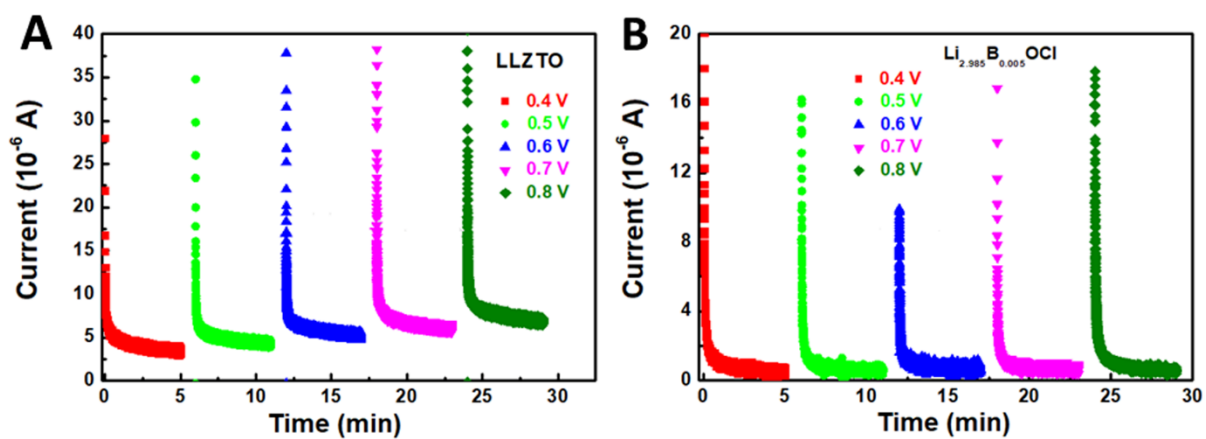**Figure S5. Direct current polarization curves of LLZTO and Li$_{2.985}$B$_{0.005}$OCl, related to Figure 3.**

(A) LLZTO at different voltages from 0.4 to 0.8 V.
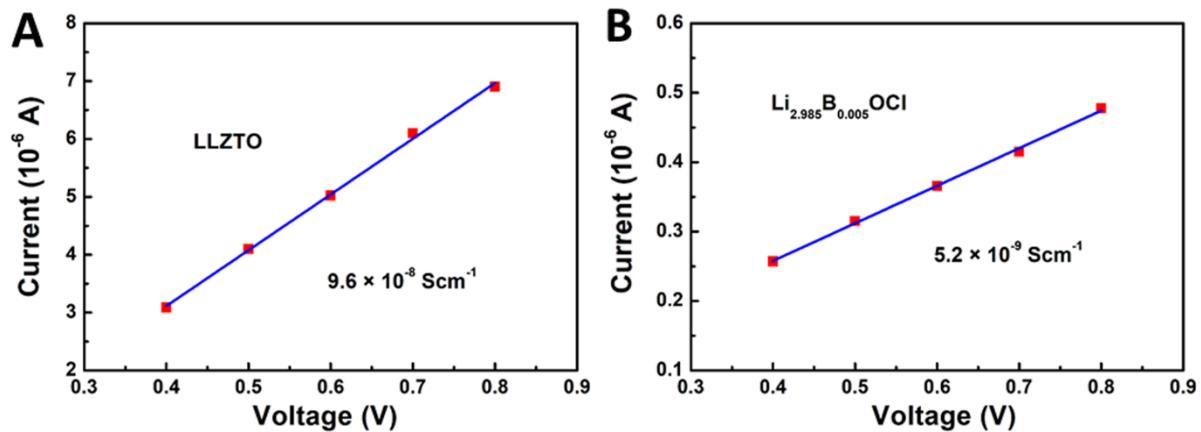
(B) Li$_{2.985}$B$_{0.005}$OCl at different voltages from 0.4 to 0.8 V.

Figure S6. Equilibrium current response of LLZTO and $Li_{2.985}B_{0.005}OCl$, related to Figure 3.

(A) LLZTO at different voltages from 0.4 to 0.8 V.

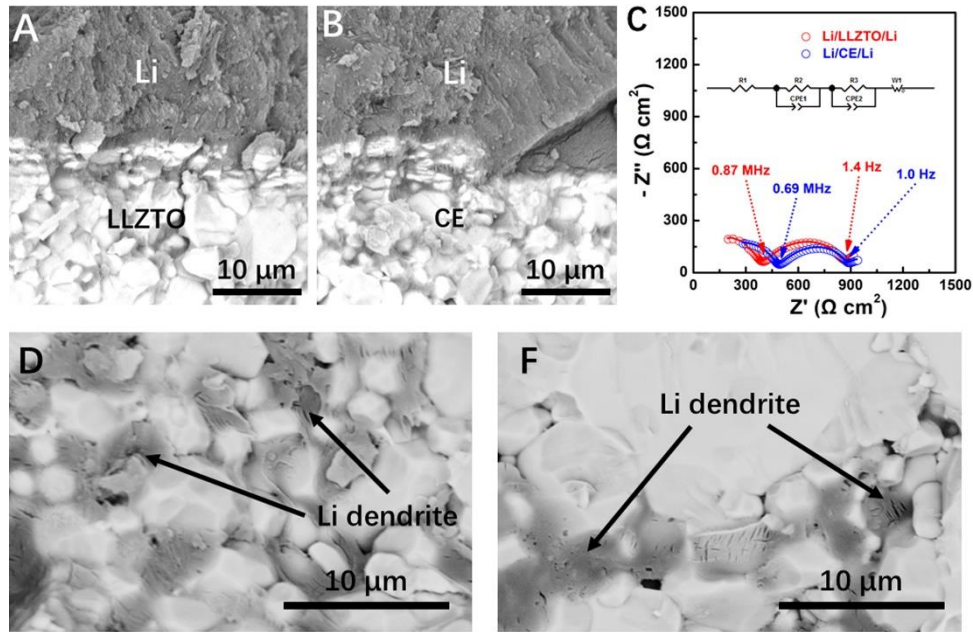(B) $Li_{2.985}B_{0.005}OCl$ at different voltages from 0.4 to 0.8 V.

Figure S7. Cross sectional SEM image, EIS profile of the Li/LLZTO/Li and Li/CE/Li symmetric cells, and the Li dendrites characterization, related to Figure 3.

(A) Cross sectional SEM image of Li/LLZTO interface.

(B) Cross sectional SEM image Li/CE interface.

(C) EIS profiles of the Li/LLZTO/Li and Li/CE/Li symmetric cells.

(D) Li dendrites characterization after CCD test, Li/LLZTO/Li.

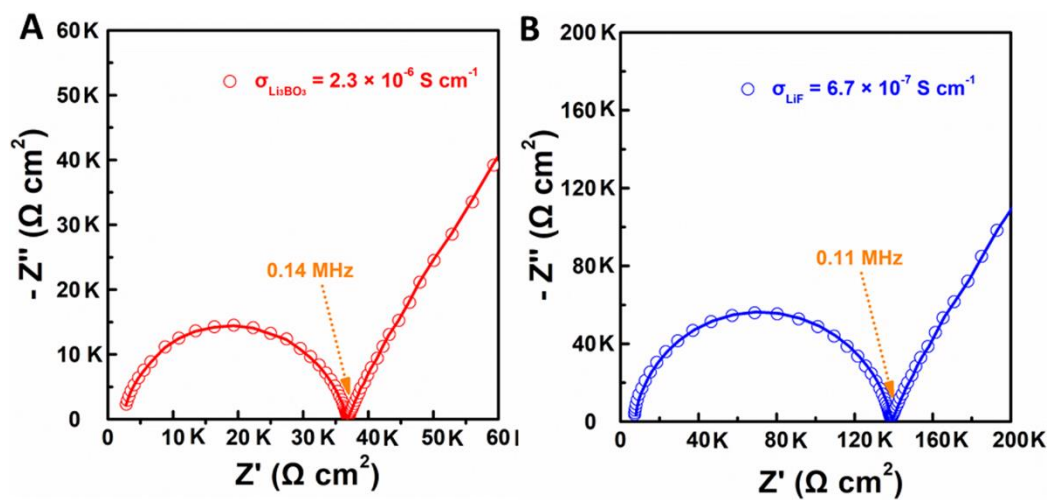(F) Li dendrites characterization after CCD test, Li/CE/Li.

Figure S8. EIS profiles of the Li_3BO_3 and LiF solders, **related to Figure 5.**

(A) EIS profile of Li_3BO_3.

(B) EIS profile of LiF.

Table S2. Assembly information and the electrochemical performance of the garnet-based bulk-type ACLBs, related to Figure 5.

| References	Solder	Li$^+$ Conductivity	Sintering Temperature	Testing Temperature	Current	Initial Coulombic Efficiency	Cycles
Park et al., 2016	Li$_3$BO$_3$	2×10^{-6} Scm^{-1}	700 °C	50 °C	0.2 C	54.7 %	10
Okumura et al., 2016	Li$_{2.2}$C$_{0.8}$B$_{0.2}$O$_3$	7.3×10^{-5}Scm^{-1}, 120 °C	660 °C	120 °C	32 μA/cm^2	80.8 %	20
Ohta et al., 2013	Li$_3$BO$_3$	2×10^{-6} Scm^{-1}	700 °C	25 °C	0.05 C	~ 85 %	5
Ohta et al., 2014	Li$_3$BO$_3$	2×10^{-6}Scm^{-1}	790 °C	25 °C	0.01 C	79.6 %	1
Han et al., 2018	Li$_{2.3}$C$_{0.7}$B$_{0.3}$O$_3$	~ 10^{-5}Scm^{-1}, 100 °C	700 °C	100 / 25 °C	0.05 C	~ 74.6 %	40
Liu et al., 2018	Li$_3$BO$_3$.In$_2$SnO$_5$	---	600-700 °C	80 °C,	10-20 μA/cm^2	~ 60 %	5
This work	Li$_{2.985}$B$_{0.005}$OCl	6.8×10^{-5}Scm^{-1}	400 °C	90 °C	0.05 C	88.6 %	50
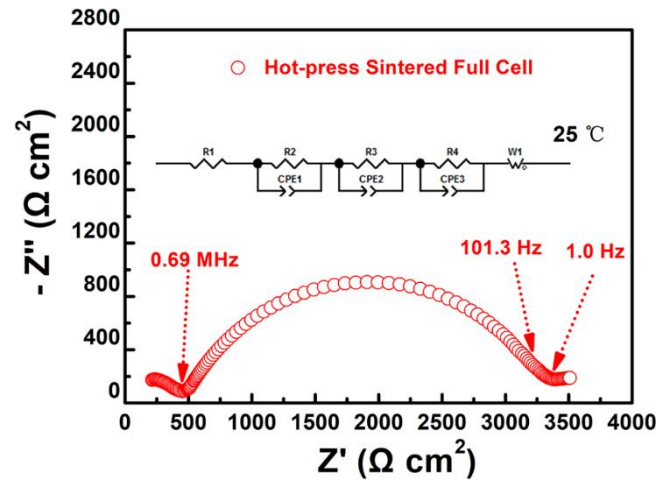
Figure S9. EIS profile of the hot-press sintered LCO/CE/Li full cells at 25 °C, related to Figure 5.

Table S3. Elasticity Modulus of the three kinds of solders, related to Figure 6.

---	$Li_{2.985}B_{0.005}OCl$	Li_3BO_3	LiF
Elasticity Modulus/GPa	7.8	20.5	11.9

Transparent Methods

In-situ coating of LLZTO@Li$_{2.985}$B$_{0.005}$OCl and LCO@Li$_{2.985}$B$_{0.005}$OCl. LLZTO powder was purchased from Kejing material technology co. LTD. In-situ coating of Li$_{2.985}$B$_{0.005}$OCl includes the dissolution of the stoichiometric amounts of LiCl, LiOH and H$_3$BO$_3$ in deionized water. The pH value of the solution was adjusted to 14 by controlling the concentration of LiOH (> 1 M). LLZTO and LCO were added into the strong basicity solution separately, then dried under agitation. The as prepared powder was sintered at 350 °C for 5 h under vacuum and then grounded in glovebox. The mass ratio of Li$_{2.985}$B$_{0.005}$OCl was controlled by adjusting the concentration of LiCl, LiOH and H$_3$BO$_3$.

Assembly of Li/LLZTO/Li and Li/CE/Li symmetric cells. The pristine LLZTO pellet was made by cold pressing under the pressure of 300 MPa and sintered at 1200 °C for 12 h with the coverage of the same mother powder. The CE pellet was made by pre-pressing under the pressure of 30 MPa in room temperature, then hot-pressed at 400 °C under 50 MPa for 1 h. A 20 nm Au modification layer was deposited on LLZTO and CE pellets by magnetron sputtering. Li foils were attached on the LLZTO and CE pellets and heated at 200 °C for 30 min under the pressure of about 5000 Pa.

Hot-pressing of the ACLBs. The cathode consists of LiCoO$_2$ active material, LLZTO electrolyte and Li$_{2.985}$B$_{0.005}$OCl solder (mass ratio = 11 : 5 : 4). Methylpyrrolidone (NMP) was added into the powder and the slurry was spin-coated on the pre-pressed CE pellet. The NMP solvent was evaporated under 80 °C and the active material loading was about 0.8 mg. The cathode was casted in a 10 mm round area and the mass ratio of the active material is 55 %, so the cathode loading can be calculated as 1.85 mg/cm^2. It should be noticed that the specific

surface area of the most of the electronic conductors are huge. The participation of the electronic conductivities will reduce the contact area of the active material with the ionic conductor, and the transportation of Li^+ will be severely restricted. Moreover, the thickness of the cathode was very thin, which had already provided an applicable electronic conductivity for the full cell. The ACLB was prepared by hot-pressing the cathode and the CE together at 400 °C for 1 h under the pressure of 50 MPa. The contrast sample, Li_3BO_3 solder were synthesized through solid reaction (ball milling the mixture of Li_2CO_3 and B_2O_3, then sintered at 600 °C for 8 h) and LiF was purchased from Alfa Aesar. Li_3BO_3 and LiF were coated on LLZTO and $LiCoO_2$ by ball milling. The mass ratio of $LiCoO_2$, LLZTO and solders were also 11 : 5 : 4, and the hot-pressing temperature were increased to 700 °C for Li_3BO_3 and 900 °C for LiF soldered counterparts.

Characterization. X-ray diffraction (XRD) data was characterized by Bruker D8 advance diffractometer by Cu Kα radiation. X-ray photoelectron spectroscopy (XPS) was carried out on RBD upgraded PHI-5000C ESCA system (PerkinElmer) with Mg Kα radiation (hv = 1253.6 eV). The structural changes, melting and solidification points of the anti-perovskites were obtained through differential scanning calorimetry (DSC, NETZSCH, Germany). The morphology of the cross sectional LLZTO and CE pellets and electrode/electrolyte interface were characterized by transmission electron microscopy (TEM, Joel JEM2010) and scanning electron microscopy (SEM, Joel JSM6390). The impedance of the electrolyte, symmetric cells and the ACLBs were measured by electrochemical impedance spectroscopy (EIS) with a frequency range from 7 MHz to 1 Hz with 50 mV perturbation amplitude. Galvanostatic stripping and plating of the symmetric cell, cyclic properties were operated on LAND

CT2001A Battery Cycler (Wuhan, China).

REFERENCES

Park, K., Yu, B.C., Jung, J.W., Li, Y.T., Zhou, W.D., Gao, H.C., Son, S., Goodenough, J.B. (2016). Electrochemical Nature of the Cathode Interface for a Solid-State Lithium-Ion Battery: Interface between $LiCoO_2$ and Garnet $Li_7La_3Zr_2O_{12}$. Chem. Mater. *28*, 8051-8059.

Okumura, T., Takeuchi, T. & Kobayashi, H. (2016). All-solid-state lithium-ion battery using $Li_{2.2}C_{0.8}B_{0.2}O_3$ electrolyte. Solid State Ionics *288*, 248-252.

Ohta, S., Komagata, S., Seki, J., Saeki, T., Morishita, S. & Asaoka, T. (2013). All-solid-state lithium ion battery using garnet-type oxide and Li_3BO_3 solid electrolytes fabricated by screen-printing. J. Power Sources *238*, 53-56.

Ohta, S., Seki, J., Yagi, Y., Kihira, Y., Tani, T. & Asaoka, T. (2014). Co-sinterable lithium garnet-type oxide electrolyte with cathode for all-solid-state lithium ion battery. J. Power Sources *265*, 40-44.

Han, F., Yue, J., Chen, C., Zhao, N., Fan, X.L., Ma, Z.H., Gao, T., Wang, F., Guo, X.X., Wang, C.S. (2018). Interphase Engineering Enabled All-Ceramic Lithium Battery. Joule *2*, 497-508.

Liu, T., Zhang, Y.B., Zhang, X., Wang, L., Zhao, S.X., Lin, Y.H., Shen, Y., Luo, J., Li, L.L., Nan, C.W. (2018). Enhanced electrochemical performance of bulk type oxide ceramic lithium batteries enabled by interface modification. J. Mater. Chem. A *6*, 4649–4657.